


Artigo

# Reliability of Operational Global Forecast System and a Local Implementation of WAVEWATCH III during an Explosive Cyclone in South America in June 2020

Marcia Carolina de Oliveira Costa<sup>1</sup>, Milton Kampel<sup>2</sup>, Vitor Galazzo de Paiva<sup>2</sup>, Rogério Batista<sup>3</sup>, Ivan Soares<sup>4</sup>, Fernando Túlio Camilo Barreto<sup>1</sup> , Douglas Fraga Rodrigues<sup>1</sup>, Carlos Leandro da Silva Junior<sup>1</sup>

<sup>1</sup>*OceanPact Serviços Marítimos, Rio de Janeiro, RJ, Brazil.*

<sup>2</sup>*Divisão de Observação da Terra e Geoinformática, Instituto Nacional de Pesquisas Espaciais, São José dos Campos, SP, Brazil.*

<sup>3</sup>*Divisão de Satélites Meteorológicos e Sensores, Instituto Nacional de Pesquisas Espaciais, Cachoeira Paulista, SP, Brazil.*

<sup>4</sup>*Atlantech Soluções Ambientais, Curitiba, PR, Brazil.*

Recebido em: 11 de Janeiro de 2023 - Aceito em: 22 de Maio de 2023

## Resumo

Ocorreu um ciclone na costa sul do Brasil entre 30/06/2020 e 01/07/2020, movendo-se do continente em direção ao mar. O sistema foi registrado em modelos numéricos e observações in-situ (boia e navio) desde o dia em que se formou até se dissipar. O objetivo deste trabalho é utilizar os dados coletados durante essa condição ambiental extrema em uma comparação estatística com o modelo atmosférico operacional Global Forecast System (GFS) e uma implementação local do modelo de ondas WAVEWATCH III (WW3), que utiliza o GFS como um dos inputs, para entender as limitações desses modelos. Inicialmente, os resultados mostraram que o sistema próximo à costa sul do Brasil era um ciclone explosivo forte de acordo com a classificação de Sanders e Gyakum (1980). Descobrimos que os modelos GFS e WW3 apresentaram maiores erros em comparação com os dados da boia durante o período de 48 horas de condições meteorológicas explosivas, enquanto para o modelo GFS, os maiores erros ao redor do navio ocorreram após esse período. Os erros do WW3 podem ser explicados pela diferença entre a profundidade da boia e o ponto da grade do WW3, e os erros do GFS nessa localização.

**Palavras-chave:** ciclones explosivos, modelos ambientais numéricos operacionais, GFS, WW3.

## Confiabilidade do Global Forecast System Operacional e uma Implementação Local do WAVEWATCH III durante um Ciclone Explosivo na América do Sul em junho de 2020

### Abstract

A cyclone occurred off the southern Brazilian coast between 30/06/2020 and 01/07/2020, moving eastwards from land towards offshore. The system was registered in numerical models and in-situ observations (buoy and ship) from the day it started until dissipated. The goal of this work is to use the data collected during this extreme environmental condition in a statistical comparison with the atmospheric operational model Global Forecast System (GFS) and a local implementation of the WAVEWATCH III (WW3) wave model, which used the GFS as one of the inputs, to understand the limitations of these models. Initially, the results showed that the system near the southern Brazilian coast was a strong explosive cyclone according to the Sanders and Gyakum (1980) classification. We found that the GFS and WW3 models exhibited greater errors when compared with the buoy data during the 48 h period of explosive weather conditions, while for the GFS model, the greatest errors around the ship occurred after that period. The WW3 errors may be explained by the difference between the buoy and WW3 gridpoint depth and the GFS errors at this location.

**Keywords:** explosive cyclones, numerical operational weather models, GFS, WW3.

## 1. Introduction

Explosive cyclone systems or “bombs” result from the rapid intensification of extra-tropical cyclones or storms (Sanders and Gyakum, 1998). The definition used by Sanders and Gyakum (1998) to quantify the pressure drop in explosive cyclones was proposed by Tor Bergeron as “the pressure variation of  $1 \text{ hPa h}^{-1}$  at lat =  $60^\circ$ , namely the threshold value of 1 Bergeron where the explosive cyclogenesis can start to happen”.

Previous research reported that the number of explosive cyclones in the period between 1979 and 1999 increased globally at a rate of 0.78 systems per year (Lim and Simmonds, 2002). Explosive cyclones can promote coastal flooding, resulting in severe economic losses and impacting coastal communities worldwide (Khalid *et al.*, 2020). The critical environmental conditions generated by these severe systems can also result in high-risk factors for maritime operations. For instance, Göksu and Arslan (2020) demonstrated that the wind speed limit for loading and unloading operations is  $\sim 11 \text{ m/s}$  (Beaufort wind force scale 5). Therefore, it is relevant to consider that numerical forecasting simulation models normally used in the planning phase of many maritime operations are capable of adequately represent environmental conditions associated with this phenomenon, especially regarding its magnitude and peak time.

Climatologically, the frequency of explosive cyclones in South America ranges from 1.57 to 2.7 systems per year with wind speeds higher than  $14 \text{ m/s}$  (Bitencourt *et al.*, 2013). However, it is still poorly understood whether a cyclone will rapidly intensify, becoming a “bomb”, and which processes control this intensification, since only a few bomb systems could be properly observed with concurrent in situ observations. Kuo *et al.* (1991) reported that explosive cyclones are typically maritime phenomena occurring mainly in the winter and are associated with regions of intense sea surface temperature gradients, suggesting that surface heat and moisture fluxes can play an important role in cyclogenesis intensification. In Brazil, extratropical cyclones are more intense and frequent off the southern Brazilian coast during the austral winter from June to August (de Lima *et al.*, 2020).

The main objectives of this study were to assess the effectiveness of a wave and an atmospheric numerical model in predicting an extreme event off the southern Brazilian coast and to determine if the cyclone system could be classified as explosive by applying the Bergeron definition. This is a rare opportunity to describe the intensification of a bomb observed between 30 June 2020 and 1 July 2020 in this region. Our characterization of the system is based on the analysis of the European Centre for Medium-Range Weather Forecasts (ECMWF) ERA5 reanalysis and an in-situ dataset.

## 2. Materials and Methods

### 2.1. Study area

The study area encompasses the Southwestern Atlantic Ocean and is bathymetrically represented by the Western Argentine Basin in the south and the Western South Atlantic Basin in the north. Both basins are separated by the Santos Plateau and the Rio Grande Rise. The central continental shelf includes portions of the southern Brazil, Uruguay, and northern Argentina shelves and extends from Cape Santa Marta Grande to Cape Corrientes ( $28^\circ \text{ S}$ - $38^\circ \text{ S}$ ) and the South Brazil Bight to the north ( $23^\circ \text{ S}$ - $28^\circ \text{ S}$ ). In the upper ocean, the water mass structure is dominated by the confluence of subtropical and subantarctic waters associated with the opposing flows of the Brazil and Malvinas Currents (Burone *et al.*, 2021). The Brazil Current flows to the south, transporting the Tropical Water (TW;  $T > 20^\circ \text{ C}$ ;  $S > 36$ ) in the mixed layer and the South Atlantic Central Water (SACW;  $T < 20^\circ \text{ C}$ ;  $35 < S < 36$ ) in the pycnocline layer (Piola *et al.*, 2018). The high temperatures of the TW are due to heat gained through the sea surface at low latitudes, while the high salinities are due to freshwater losses to the atmosphere at mid-latitudes, where evaporation greatly exceeds precipitation (Piola and Matano, 2019). The Coastal Water with low salinity (CW;  $S < 35$ ) mainly occupies the inner shelf (Castro and Miranda, 1998). The upper layer of the Malvinas (or Falkland) Current is substantially colder ( $T < 15^\circ \text{ C}$ ) and fresher ( $S < 34.2$ ) than the corresponding layer of the Brazil Current. These properties reflect the subantarctic origin of the Malvinas Current waters. In the austral winter, intrusions to the north of low salinity waters from the south off the Río de la Plata, Patos, and Mirim Lagoons intrude into the Southern and Southeastern shelves of Brazil (Möller *et al.*, 2008; Piola *et al.*, 2000; Stevenson *et al.*, 1998) (Fig. 1).

The meteorological conditions in the study region are affected mainly by frontal systems, mesoscale convective systems, cyclonic systems at medium levels of the atmosphere, upper-level cyclonic vortices, and cyclones (Cavalcanti *et al.*, 2009). This region is also a cyclogenetic area where extra-tropical cyclones are formed (Hoskins and Hodges, 2005). Based on available wave data, Cuchiara *et al.* (2009) indicated that the predominant wave directions in the Southern Brazilian continental shelf are  $100^\circ$  and  $160^\circ$  (E-SE), while the wave heights vary from 1 to 1.5 m. Regarding the wave period, a variation between 6 and 14 s was observed. Although winter is the most energetic season in the study region, significant wave height ( $H_s$ ) higher than 4 m is present in all seasons (Araujo *et al.*, 2003). Furthermore, despite its microtidal regime, the maximum values of both  $H_s$  and storm surges are found in this region because of its high exposure to frequent and intense extratropical storms (Ohz *et al.*, 2020; Rodríguez *et al.*, 2016).

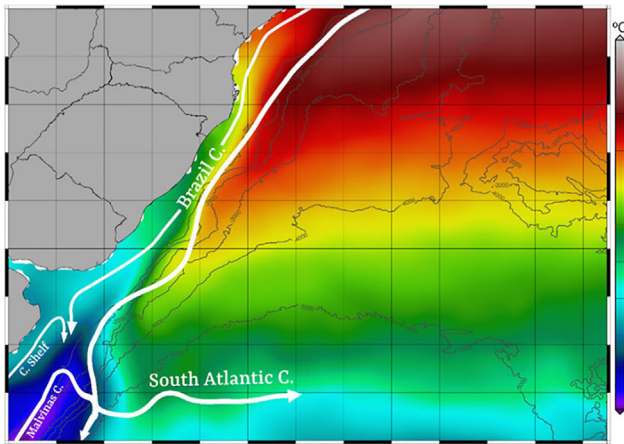


**Figure 1** - Map showing the location of the study area. ERA5 sea surface temperature climatology for July (1979-2020) and schematic representation of the main upper ocean circulation in the Southwestern Atlantic Ocean (isobaths in black).

## 2.2. Data

### 2.2.1. ERA5 Reanalysis

The ERA5 dataset was developed by the Copernicus Climate Change Service, implemented by the European Centre for Medium-Range Weather Forecasts (ECMWF). The reanalysis was produced by combining short-term numerical predictions with observational data. ERA5 is produced using the assimilation of atmosphere and surface data in four dimensions through the ECMWF Integrated Forecast System with 137 vertical levels in sigma coordinates (which use atmospheric pressure on the surface as a reference) in grids with a 31 km resolution for atmospheric levels and  $\sim 55$  km resolution for wave data. Hourly ERA5 data are available for several atmospheric and oceanic variables, including sea level pressure (SLP), sea surface temperature (SST), wind speed (WS), and significant wave height (Hs). Data were obtained for the period from 29 June to 4 July 2020 (Table 1).

### 2.2.2. Global forecast system

The Global Forecast System (GFS) is a weather forecast model produced by the National Centers for Environmental Prediction (NCEP). This model covers the entire globe with a horizontal resolution of 28 km between gridpoints up to 16 days in the future. We used the GFS forecasts with a spatial resolution of  $0.5^\circ \times 0.5^\circ$  (55 km) and a temporal resolution of 3 h (NOAA).

### 2.2.3. WAVEWATCH III

The WAVEWATCH III (WW3) wave model, version 5.16, released by NOAA on 31 October 2016, was used in the present study. WW3 is an open-source model available under request from NOAA. WAVEWATCH III<sup>®</sup> (Tolman, 1997; Tolman, 2009) is a third-generation wave model developed at NOAA/NCEP (Komen *et al.*, 1994; WAM-

**Table 1** - Main characteristics of the reanalysis, numerical models, and in situ datasets used in the study.

Dataset		Temporal resolution	Spatial resolution	Variable
Reanalysis	ERA5	1 h	31 km ( $0.25^\circ \times 0.25^\circ$ )	SLP, SST, WS
			55 km ( $0.5^\circ \times 0.5^\circ$ )	Hs
Numerical model	WW3	1 h	14 km ( $0.125^\circ \times 0.125^\circ$ )	Hs, Tp
	GFS	3 h	55 km ( $0.5^\circ \times 0.5^\circ$ )	SLP, WS
In situ	Buoy	1 min	-	SLP, WS, Hs, Tp
	Ship	1 min	10 m	WS

SLP - sea level pressure, SST-sea surface temperature, WS - wind speed, Hs - significant wave height, Tp - wave peak period, WW3 - WAVEWATCH III model, GFS - Global Forecast System.

DIG, 1988). It is a further development of the WAVEWATCH model developed at Delft University of Technology (Tolman, 1997; Tolman, 2009) and the WAVEWATCH II model developed at the NASA Goddard Space Flight Center (For details, please see Tolman, 1997; Tolman, 2009).

The WW3 model was configured to run in two nested numerical grids (Fig. 2) from a 3 h GFS operational model, while the outputs were produced in 1 h time steps. The larger grid has a resolution of  $0.5^\circ \times 0.5^\circ$ , spanning the entire Atlantic Ocean. A second grid spans the Brazilian coast with a spatial resolution of  $0.125^\circ \times 0.125^\circ$ . The directional resolution was  $15^\circ$  and the frequency space was 0.0417 Hz to 1.0 Hz, with a frequency resolution of 0.04 Hz. The simulation started two months before the event.

This configuration was chosen to minimize the influence of the open-boundary conditions, as the boundaries of the Atlantic Ocean grid are far from the study region in the Southwestern Atlantic. Therefore, the open boundaries are prepared to radiate the inner waves without any incoming waves. The Brazilian grid receive their open-boundary values from the larger grid, where it is nested. Global ETOPO-1 bathymetry at a 1 min spatial resolution was interpolated for the different resolutions of each WW3 numerical grid. In coastal areas, the ETOPO-1 bathymetry was merged with local navigation charts. A Shapiro filter was used for removing small spurious gradients introduced in the merging process. This filter acts only in the locality where the gradients are significantly high.

## 2.3. In situ data

Significant wave height, peak period (Tp), wind speed, and sea level pressure data measured from 24

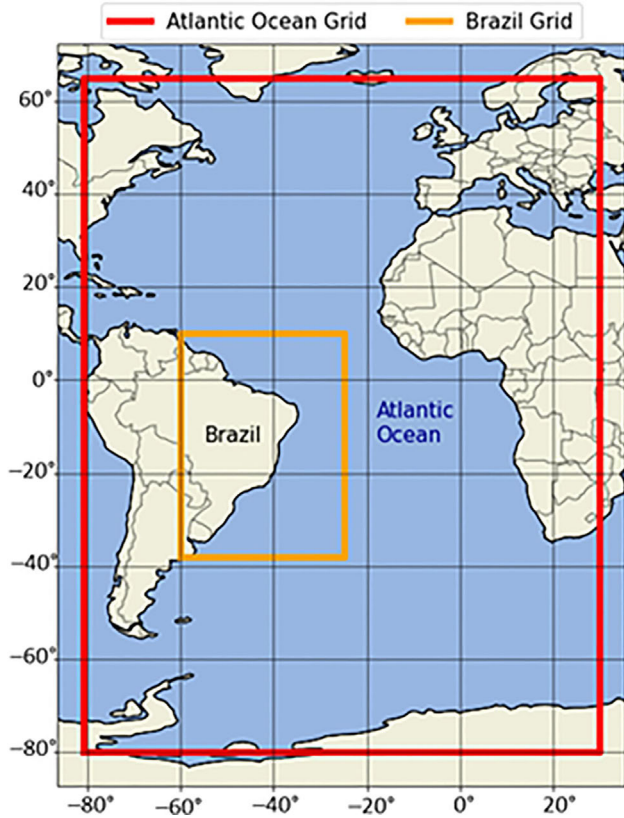


**Figure 2** - Configuration of the two nested grids for running the WAVEWATCH III (WW3) model: the Atlantic Ocean grid ( $0.5^\circ \times 0.5^\circ$ ) in red and the Brazilian grid ( $0.125^\circ \times 0.125^\circ$ ) in orange (see text for details?).

June to 09 July 2020 in a buoy moored at  $32.3^\circ$  S- $52.1^\circ$  W (14 m depth) were obtained from the Brazilian Coast Monitoring System (<https://simcosta.furg.br/home>). Wind speed data measured from 29 June to 2 July 2020 by a Gill WindObserver II anemometer installed on a research ship at  $26.45^\circ$  S- $46.68^\circ$  W were obtained from OceanPact Maritime Services Corporation.

## 2.4. Classification of cyclone intensity

According to Sanders and Gyakum (1980), a system is considered an explosive cyclone when the central pressure falls at a rate of at least 1 mb/h for 24 h, at  $60^\circ$  latitude. In order to identify if/when the system could be classified as explosive, the deepening rate ( $DR$ ) was calculated on an hourly basis (Eq. (1)), using the minimum SLP ERA5 values as the central pressure ( $P_c$ ) of the cyclone system. The temporal evolution of  $P_c$  allowed tracking the development and the path of the cyclone. The cyclone 24 h deepening rate ( $CDR$ ) was computed using Eq. (2), corrected by the mean latitude of the system over 24 h:

$$DR = \frac{P(t+1\text{ h}) - P(t) \sin 60^\circ}{1\text{ hPa} \sin \phi} \quad (1)$$

$$CDR = \frac{\Delta P \sin 60^\circ}{24\text{ h} \sin \phi} \quad (2)$$

where  $P$  is the central pressure at time  $t$ ,  $\Delta P$  is the variation of the cyclone central pressure in 24 h, and  $\phi$  is the mean latitude of the system, considering the initial and final positions over 24 h.

## 2.5. NWP statistical analysis

The bias (Eq. (3)) and mean absolute error (MAE) (Eq. (4)) were calculated to assess the effectiveness of the numerical weather prediction models (NWP) previously mentioned (WW3 and GFS), comparing SLP, WS, Hs, and Tp against the hourly average buoy/ship in situ data. The comparisons used the NWP's outputs located at the nearest gridpoint to the buoy ( $32.5^\circ$  S- $52.0^\circ$  W, 20 m depth) and to the ship's ( $26.5^\circ$  S- $46.5^\circ$  W) positions.

$$BIAS = \frac{1}{n} \sum_{j=1}^n (a_j - \hat{a}_j) \quad (3)$$

$$MAE = \frac{1}{n} \sum_{j=1}^n |a_j - \hat{a}_j| \quad (4)$$

where  $a$  and  $\hat{a}$  are the environmental conditions predicted and measured, respectively, at timestep  $j$  in a set of  $n$  elements.

## 3. Results

### 3.1. Cyclone description

On land, the system moved eastwards until it reached the ocean ( $33.1^\circ$  S- $52.5^\circ$  W) on 30 June 2020 12:00 (all times in UTC), and then moved eastwards between  $34.3^\circ$  S and  $37.5^\circ$  S (Figs. 3 and 4). Figure 3 shows that the cyclone generated winds stronger than 14 m/s in a radius that varied between 1200 km and 1500 km. Along the coast, the system caused a variation in wind direction from northeast to southwest between 30 June at 12:00 and 01 July 2020 at 12:00. Considering  $35.9^\circ$  S as the mean latitude, 1 Bergeron represents a drop of  $\sim 15.6$  hPa in 24 h (or 0.65 hPa/h). Even with deepening rates  $>1$  Bergeron before 30 June 2020, continuous explosive deepening pressure was observed only after the system reached the ocean (Fig. 5). Therefore, the 24 h deepening rate was calculated using the 24 h difference of the minimum SLP between 30 June 2020 at 12:00 and 01 July 2020 at 12:00 (35.3 hPa), resulting in a deepening rate of 2.28 Bergerons. This classified the system as a strong explosive cyclone according to the Sanders and Gyakum (1980) classification. After 8 h over colder

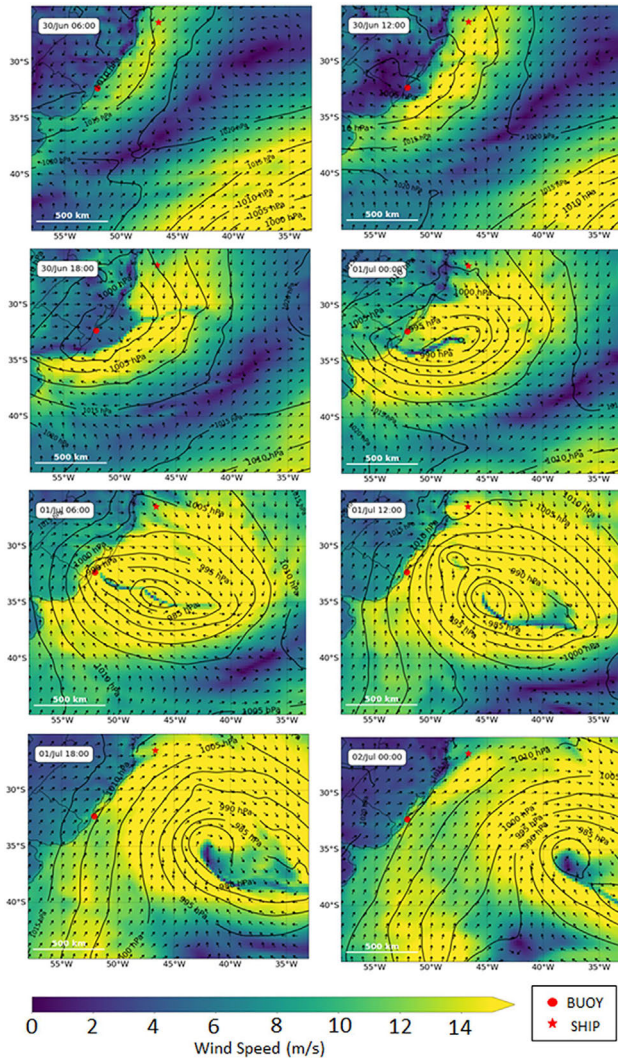


**Figure 3** - ERA5 wind speed and sea level pressure fields between 30 June 2020 at 12:00 and 02 July 2020 at 06:00 UTC.

coastal waters ( $<15^{\circ}\text{C}$ ), the cyclone crossed a sea surface temperature (SST) gradient into warmer oceanic waters of the Brazil Current ( $>20^{\circ}\text{C}$ ), while the hourly deepening rate increased twofold. Maximum wind speed ( $W_{\text{max}}$ ) increased from 30 June 2020 at 00:00, reaching its highest values on 01 June 2020 ( $>27.5\text{ m/s}$ ). The maximum significant wave height ( $H_{\text{s max}}$ ) showed a similar pattern as the maximum wind speed (Fig. 5).

### 3.2. NWP statistical analysis

Table 2 shows the statistical comparison between NWP forecasts and in situ data. At the buoy location, the GFS slightly overestimated the WS (bias 0.70 m/s, MAE 1.46 m/s) and underestimated SLP (bias -1.07 hPa, MAE 1.44 hPa) from 25 June 2020 at 00:00 to 09 July 2020 at 00:00. However, at the nearest gridpoint to the ship, the GFS underestimated the WS (bias -0.18 m/s, MAE

**Table 2** - Numerical weather prediction model (NWP) statistical analysis compared with buoy and ship in situ data.

In Situ Data	NWP	Bias	MAE	Period analyzed
Buoy	GFS WS	0.70 m/s	1.46 m/s	25 June, 00:00, to 09 July 2020, 00:00
Ship	GFS WS	-0.18 m/s	0.21 m/s	27 June, 00:00, to 09 July 2020, 00:00
Buoy	GFS SLP	-1.07 hPa	1.44 hPa	25 June, 00:00, to 09 July 2020, 00:00
Buoy	WW3 Hs	-0.005 m	0.21 m	25 June, 00:00, to 09 July 2020, 00:00
Buoy	WW3 Tp	-0.53 s	1.58 s	25 June, 00:00, to 09 July 2020, 00:00

0.21 m/s), from 27 June 2020 at 00:00 to 9 July 2020 at 00:00. WW3 underestimated both Hs (bias -0.005 m, MAE 0.21 m) and Tp (bias -0.53 s; MAE 1.58 s) from 25 June 2020 at 00:00 to 09 July 2020 at 00:00.

To better assess the effectiveness of the NWPs to predict extreme environmental conditions during the explosive cyclone event, the bias and MAE analysis were also computed as follows: (1) First period - before the DR became explosive (from 25 June 2020 at 00:00 to 30 June 2020 at 11:00), (2) Second period – 48 h after the hourly deepening rate (DR) became explosive (from 30 June 2020 at 12:00 to 02 July 2020 at 12:00), and (3) Third period - after 02 July 2020 at 12:00. The second period (2) is referred as “extreme weather period”.

### 3.3. Temporal window comparison of GFS vs. In situ data

During the first period (1), the GFS overestimated the buoy WS (bias 0.86 m/s, MAE 1.20 m/s) (Fig. 6, right) and underestimated the ship WS (bias -0.83, MAE 1.39 m/s) (Fig. 7, right). During the extreme weather period (2), the GFS underestimated the buoy WS (bias -0.20 m/s, MAE 2.00 m/s) and overestimated the ship WS (bias 0.19 m/s, MAE 1.42 m/s). During the third period (3), the GFS overestimated both the buoy WS (0.88 m/s, MAE 1.52 m/s) and the ship WS (bias 0.04 m/s, MAE 1.70 m/s).

Regarding SLP, the GFS underestimated buoy measurements (bias -0.19 hPa, MAE 1.01 hPa) during the first period (1). During the explosive period (2), the GFS underestimated the buoy SLP more strongly (bias -2.18 hPa, MAE 3.28 hPa), and during the third period, the GFS underestimated the buoy SLP (bias -2.00 hPa, MAE 2.01 hPa) (Fig. 8).

### 3.4. Temporal window comparison of WW3 vs. In situ data

Figure 9 shows the temporal series of Hs measured by the buoy and predicted by WW3 at the nearest grid-

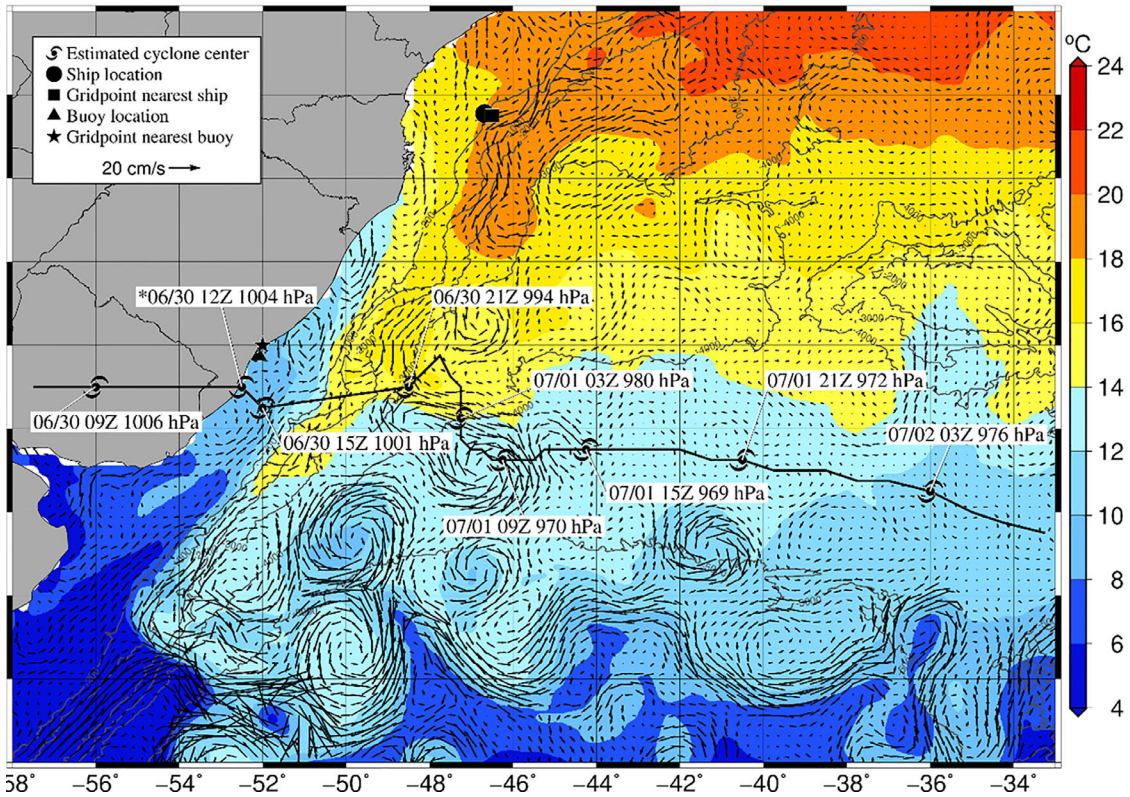


**Figure 4** - Cyclone path over mean ERA5 sea surface temperature (from 30 June 2020 to 02 July 2020) and surface ocean circulation (from 28 June 2020 to 04 July 2020).

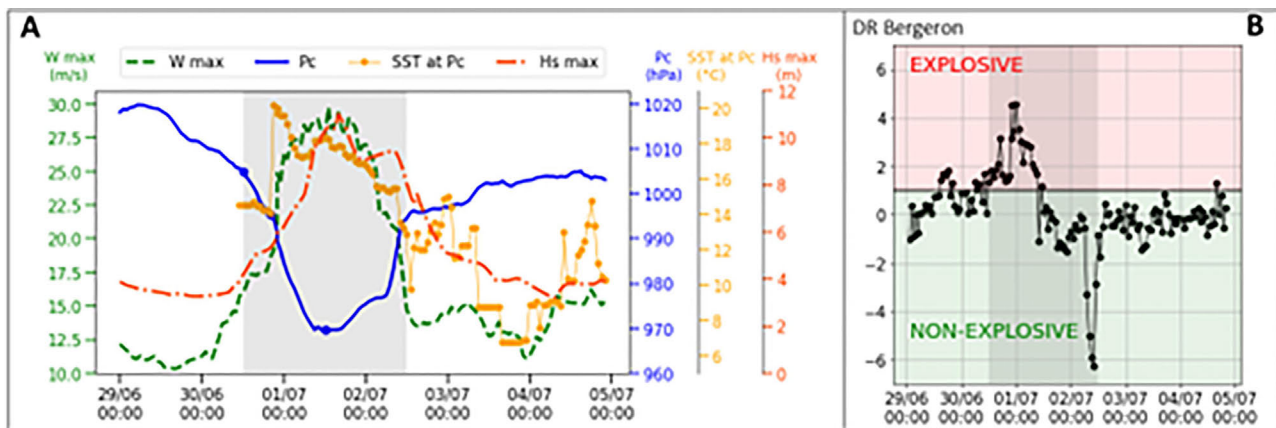


**Figure 5** - (A) Minimum sea level pressure (Pc), sea surface temperature (SST) at Pc, maximum significant wave height (Hs max), and maximum wind speed (WS max) from 29 June 2020 at 00:00 to 05 July 2020 at 00:00 (Data source: ERA5). The grey area comprises the 48 h after the hourly deepening rate (DR) became explosive. (B) Hourly deepening rate of Pc (DR) at the mean latitude between consecutive centre pressures.

point to the buoy between 25 June 2020 and 09 July 2020. During the first period (1), the WW3 forecast overestimated the buoy Hs (bias 0.06 m, MAE 0.11 m). During the extreme weather period (2), WW3 underestimated Hs (bias -0.51 m, MAE 0.71 m). During the third period (3), WW3 overestimated the Hs (bias 0.09 m, MAE 0.16 m). In general, WW3 underestimated the Tp (Fig. 10), during the first nonexplosive period (bias -0.11 s, MAE 1.27 s),

the explosive period (bias -1.82 s, MAE 2.83 s), and the third nonexplosive period (bias -0.56 s, MAE 1.52 s).

#### 4. Discussion

Strong explosive cyclones, such as the one described in this study, represent 2.5% of all explosive cyclones on the eastern coast of South America (Bitencourt *et al.*,

2013). The system examined here started over the continent but demonstrated explosive development when it

moved to the ocean. Bitencourt *et al.* (2013) showed that 23.5% of all explosive cyclones in South America start

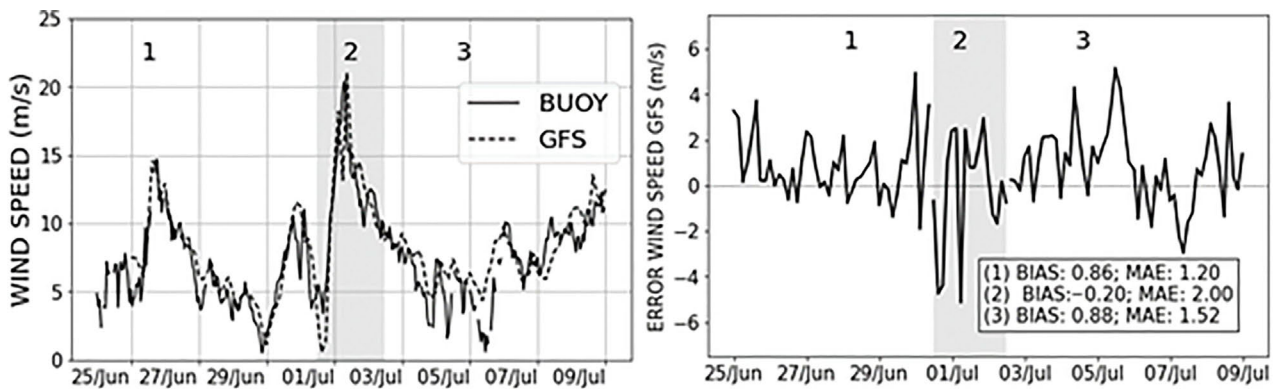


**Figure 6** - Left: wind speed records of the buoy (solid line) and predicted by the GFS (dashed line) at the nearest gridpoint to the buoy location (32.3° S-52.1° W). Right: wind speed error between the GFS predictions and buoy measurements; bias and MAE were calculated for the following temporal windows: (1) First period from 25 June 2020 at 00:00 to 30 June 2020 at 11:00; (2) 48 h after the DR became explosive, from 30 June 2020 at 12:00 to 02 July 2020 at 12:00; (3) third period after 02 July 2020 at 12:00.

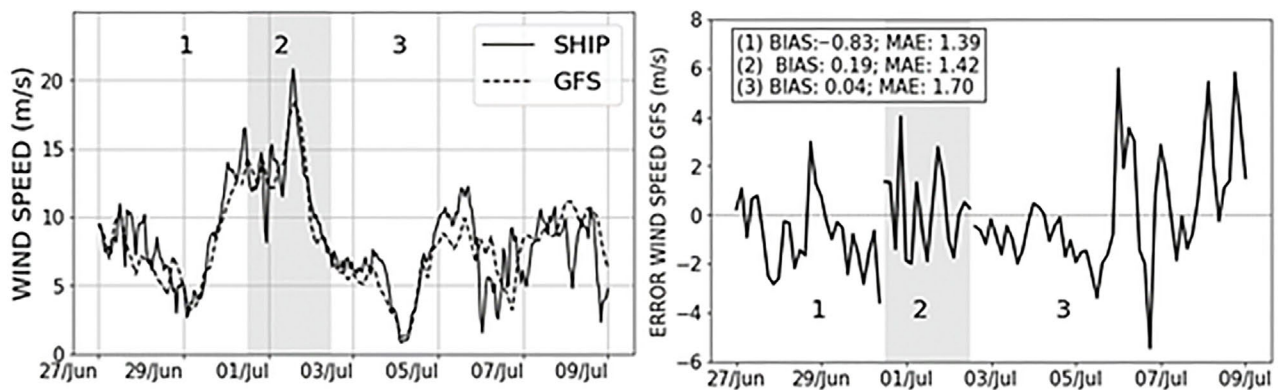


**Figure 7** - Left: wind speed records of the ship (solid line) and predicted by the GFS (dashed line) at the nearest gridpoint to the ship location (26.45° S-46.68° W). Right: wind speed error between the GFS predictions and ship measurements; bias and MAE were calculated for the following temporal windows: (1) first period from 27 June 2020 at 00:00 to 30 June 2020 at 11:00; (2) 48 h after the DR became explosive, from 30 June 2020 at 12:00 to 02 July 2020 at 12:00; and (3) third period after 02 July 2020 at 12:00.

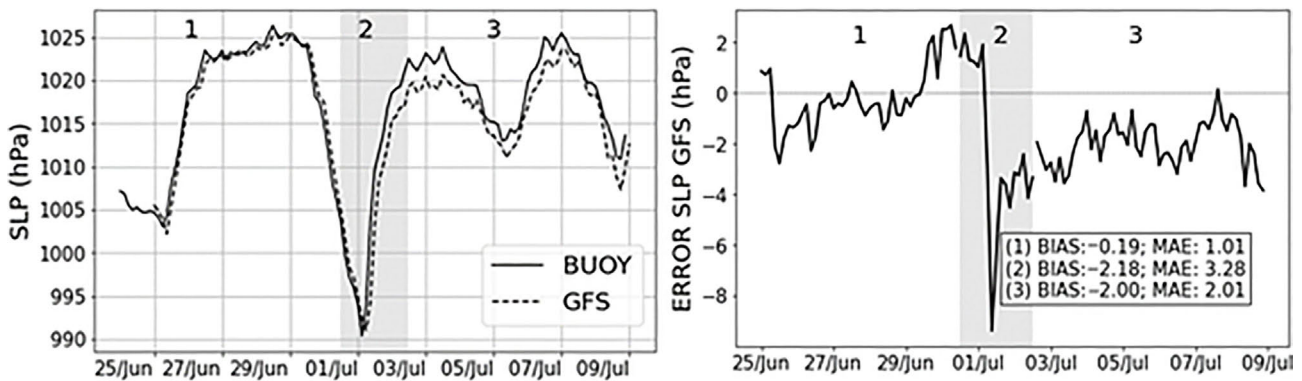


**Figure 8** - Left: sea level pressure (SLP) records of the buoy (solid line) and predicted by the GFS (dashed line) at the nearest gridpoint to the buoy location (32.3° S-52.1° W). Right: SLP error between the GFS s and buoy measurements; bias and MAE were calculated for the following temporal windows: (1) first period from 25 June 2020 at 00:00 to 30 June 2020 at 11:00; (2) 48 h after the DR became explosive, from 30 June 2020 at 12:00 to 02 July 2020 at 12:00; and (3) third period after 02 July 2020 at 12:00.

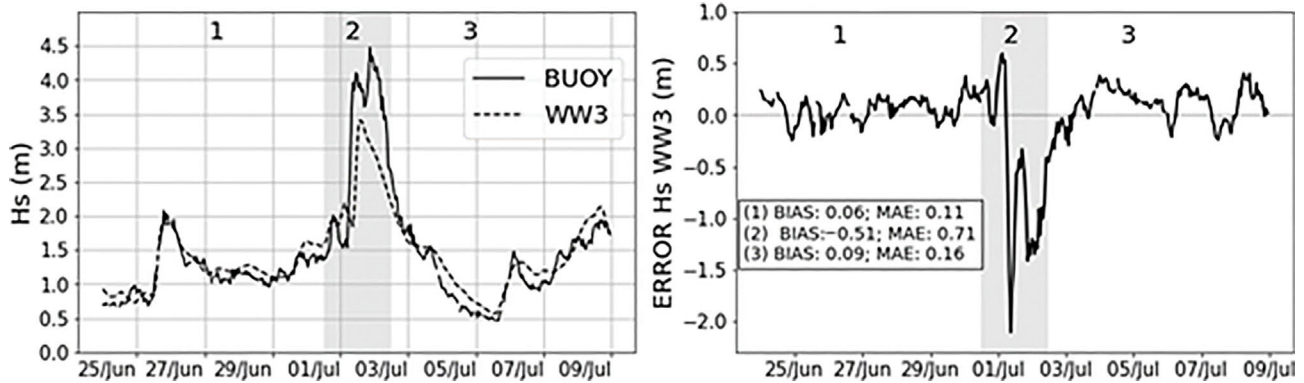


**Figure 9** - Left: significant wave height (Hs) records of the buoy (solid line) and predicted by WW3 (dashed line) at the nearest gridpoint to the buoy location ( $32.3^{\circ}$  S- $52.1^{\circ}$  W). Right: Hs error between the WW3 predictions and buoy measurements; bias and MAE were calculated for the following temporal windows: (1) nonexplosive weather from 25 June 2020 at 00:00 to 30 June 2020 at 11:00; (2) 48 h after the DR became explosive, from 30 June 2020 at 12:00 to 02 July 2020 at 12:00; and (3) nonexplosive weather after 02 July 2020 at 12:00.

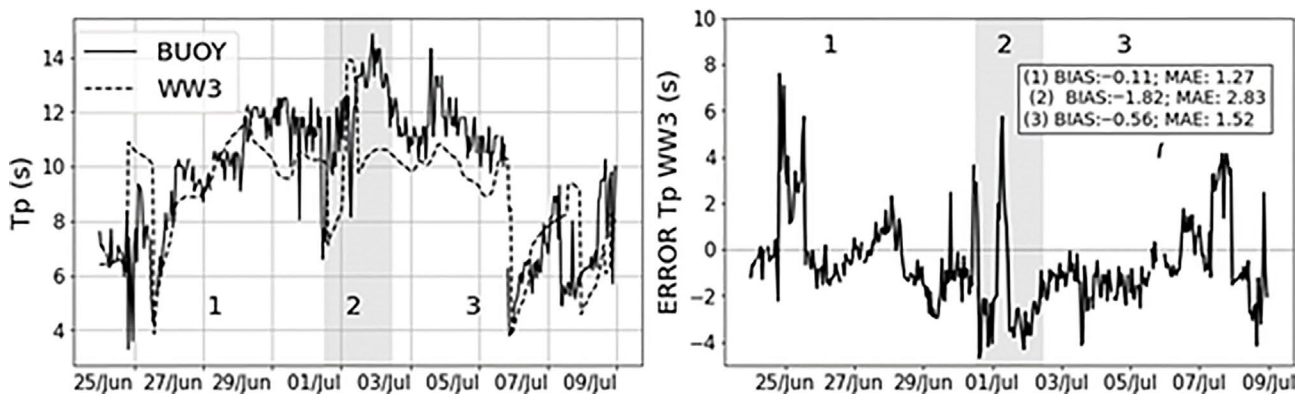


**Figure 10** - Left: wave peak period (Tp) records of the buoy (solid line) and predicted by WW3 (dashed line) at the nearest gridpoint to the buoy location ( $32.3^{\circ}$  S- $52.1^{\circ}$  W). Right: Tp error between the WW3 predictions and buoy measurements; bias and MAE were calculated for the following temporal windows: (1) nonexplosive weather from 25 June 2020 at 00:00 to 30 June 2020 at 11:00; (2) 48 h after the DR became explosive, from 30 June 2020 at 12:00 to 02 July 2020 at 12:00; and (3) nonexplosive weather after 02 July 2020 at 12:00.

their cyclogenesis over the continent, but they are considered explosive only over the ocean. It is known that sea surface temperature directly affects the air boundary layer, favoring vertical instability (stability) of the atmosphere over warm (cold) waters, which increases (decreases) wind intensity (Wallace *et al.*, 1989). This mechanism has been previously described by other authors regarding the air-sea interactions on the Brazil Malvinas Confluence (Camargo *et al.*, 2013; Pezzi *et al.*, 2005, Pezzi *et al.*, 2009, Tokinaga *et al.*, 2005). In fact, the hourly deepening rate indicated that the cyclone intensified more after crossing an SST gradient ( $\sim 5^{\circ}\text{C}/416\text{ km}$ ) from colder to warmer waters. This cyclone intensification was also reflected in the rate of wind speed increase. During the 8 h over colder waters, the maximum WS increased at a rate of  $\sim 17\%$ , which contrasts with the increase rate of  $\sim 43\%$  for the next 8 h after the system crossed into warmer waters. Although this pattern could be associated with heat fluxes during cyclone intensification, several studies have repor-

ted that these fluxes have a secondary role, whereas the latent heat accumulated 24 h prior to the fastest deepening is crucial to “bomb” development (e.g., Bui and Spengler, 2021; Gyakum and Danielson, 2000; Kuo *et al.*, 1991; Seluchi and Saulo, 1998; Tsopouridis *et al.*, 2020).

The results presented in the previous sections indicated that compared with buoy data, the NWP forecasts exhibited the largest differences 48 h after the DR became explosive (window 2), while for ship data, the largest differences were seen during the nonexplosive weather after the bomb (window 3). The GFS WS MAE at the buoy during explosive weather was 1.66 and 1.32 times larger than that of the nonexplosive weather window before (1) and after (3) the extreme event (2). For the GFS WS at the ship, the MAE during explosive weather was 1.02 higher than that of window 1 and 1.19 smaller than that of nonexplosive weather (3). The GFS SLP MAE compared with the buoy data during explosive weather was 3.25 and 1.63 times larger than that of nonexplosive weather (1 and



3, respectively). For the WW3 Hs compared with the buoy data, the MAE during nonexplosive weather (1) was 6.5 times smaller than that of window 2, while the MAE in window 3 was 4.4 times smaller than that of explosive weather. The WW3 MAE for Tp during explosive weather was 2.23 and 1.86 higher than that of the nonexplosive windows (1 and 3, respectively).

The statistical parameters (bias and MAE) calculated for the whole series (Section 3.2) were strongly influenced by the distinct pattern within the three temporal windows here analyzed (1, 2, and 3). This pattern shows the relevance of assessing NWP forecast performance during extreme events separately from more typical conditions. A previous modeling study in the same study area reported different root mean square error for comparisons of the real-time wave forecast under normal weather conditions (0.68 m) and extreme weather (1.55 m) against in situ buoy measurements (Khalid *et al.*, 2020).

The GFS WS exhibited distinct bias patterns compared with the buoy and ship measurements within temporal windows 1, 2, and 3. First, this could be related to the distance between the buoy and the ship (860 km). As shown in Figs. 3 and 4, the buoy was closer to the track of central pressure (minimum distance to central pressure: 92 km on 30 June 2020 at 12:00) than the ship (minimum distance to central pressure: 640 km on 30 June 2020 at 23:00). Because of this, the cyclone affected each location differently, causing greater SLP variation between calm and extreme weather at the buoy (Fig. 3), which caused the wind speed at the buoy to increase more sharply than at the ship (Figs. 3, 7, and 8). In addition, GFS WS had a 2 h delay for the maximum wind speed at the buoy, which was not found at the gridpoint compared against the ship. A delay of 3 h was also found during extreme weather for the minimum GFS SLP at the buoy location. This indicates that the GFS at the buoy position had a delay in representing the explosive cyclone. Khalid *et al.* (2020) also reported an overestimation of the GFS WS forecasts compared with the in situ coastal meteorological station data in the southernmost stations, as opposed to the underestimation of the GFS WS compared with other stations along the Brazilian coast during the same period. The authors attributed these differences to the absence of reduction features, such as buildings or trees, in the current GFS modeling domain. In the present study, the in situ WS buoy data were acquired in a coastal area; hence, it is possible that the GFS at this location could be under similar limitations as reported by Khalid *et al.* (2020).

According to buoy data, Hs intensification started on 01 July 2020 at 05:00, while WW3 predicted this increase 4 h later, on 01 July 2020 at 09:00 (Fig. 9), also showing the highest Hs difference (~2.10 m). During explosive weather, two Hs peaks were registered by the buoy, the first on 01 July 2020 at 11:00 (4.1 m), and the second 10 hours later (4.47 m). However, WW3 only predicted

one Hs peak on 01 July 2020 at 14:00 (3.40 m), followed by a continuous Hs attenuation. WW3 also predicted a Tp of >12 s for only 7 h (from 01 July 2020 at 04:00 to 01 July 2020 at 11:00), whereas buoy measurements registered a Tp of >12 s for a longer period, from 01 June 2020 at 09:00 to 02 July 2020 at 15:00 (30 h). Hence, WW3 predicted extreme sea states during the cyclone for fewer hours compared with the buoy records.

The increase in WW3 WS bias and MAE during the extreme weather period was greater than that of the GFS, which was expected since the GFS is used as an input for WW3, possibly causing GFS error accumulation and other constraints of WW3 itself. Wilcken (2012) pointed out that uncertainties of wave forecasts, which are the most important forecast in most maritime operations, are possibly larger than the uncertainties of atmospheric forecasts because numerical wave models use atmospheric modeling outputs as inputs for wave prediction. For instance, the delay in WW3 for extreme conditions of Hs (4 h) was twice the delay of the GFS for WS. Another source of uncertainty of the WW3 forecast could be the spatial difference between the model gridpoint (20 m depth) and the buoy mooring location (14 m depth). Thus, the slight overestimation of the WW3 Hs during calm weather could be explained by the joint effect of wind speed overestimation and depth difference. However, although both GFS WS and WW3 Hs had negative bias during explosive weather, the substantial rise in WW3 Hs MAE may indicate that during this period, the model errors could have been caused by other constraints. For example, previous studies showed that analytical spectra used in wave modeling, such as the Joint North Sea Wave Observation Project (JONSWAP) approach used for the WW3 setup in the present study, may not resemble properly mixed seas conditions or multi-modal spectra that are commonly observed at sea (Guachamin-Acero *et al.*, 2016; Guachamin-Acero and Li, 2018). Therefore, this type of approach may result in a misrepresentation of the actual wave spectra in the study area, introducing large uncertainty that could be critical to the planning phase of maritime operations (Guachamin-Acero *et al.*, 2016; Guachamin-Acero and Li, 2018). Similarly, the WW3 forecast strongly underestimated the Tp during the extreme weather period, with some errors of ~4 s (Fig. 10). These deviations in Hs and Tp represent strong evidence that the sea states were misrepresented by the WW3 in the study area during the explosive cyclone here analyzed. Another indication that the WW3 errors during window 2 could be related to the absence of different sea states prediction by the model is the lack of two Hs peaks during the explosive weather registered by the buoy.

Uncertainties, such as a delay of 4 h in wave increase in the weather window calculation could be catastrophic, with financial and environmental costs and loss of life. Göksu and Arslan (2020) showed that ship operations,

such as loading and discharging, must be carried out with maximum care when wind force is above 6 Beaufort (i.e., wind speed between 11 and 14 m/s and wave height between 3 and 4 m). Even weather and sea states that represent relatively low potential hazards may cause risk for operational activities under certain sea conditions (Zhang and Li, 2017). To deal with uncertainties in predicted environmental conditions in the planning phase of maritime operations, DNV (2011) recommends the reduction of operational limits by alpha factors. These alpha factors are basically calculated by comparing the forecasted wave height and wind speed against actual measurements (Guachamin-Acero and Li, 2018). However, considering the different performances of the forecasts during calm and extreme conditions as shown here, the use of a fixed value to reduce the operational limit could be considered unsuitable. A possible solution for this pattern could be defining two alpha factors: one for extreme weather conditions and another for the daily sea state. Another methodology to calculate  $H_s$  and  $T_p$  operational limits was proposed by Guachamin-Acero and Lin (Guachamin-Acero and Li, 2018). This approach is more reliable for scenarios such as the one described here since it aims to consider uncertainties in wave spectral energy distribution at an offshore site.

## 5. Conclusions

The results presented here showed that the system that occurred near the southern Brazilian coast on 01 July 2020 was a strong explosive cyclone according to the Sanders and Gyakum (1980) classification and began its explosive behavior after reaching the ocean. Furthermore, the cyclone deepening rate intensified after the system crossed over an SST gradient ( $\sim 5^\circ\text{C}/416\text{ km}$ ) from colder to warmer waters. At the nearest gridpoint to the buoy ( $32.3^\circ\text{ S}-52.1^\circ\text{ W}$ ), the GFS (wind speed and SLP) and WW3 ( $H_s$  and  $T_p$ ) exhibited greater constraints during the 48 h explosive weather condition. On the other hand, the GFS wind speed close to the ship ( $26.45^\circ\text{ S} - 46.68^\circ\text{ W}$ ) had the largest error in the period after the 48 h period of explosive weather. Although some of the WW3 errors may be explained by the difference between the buoy and WW3 gridpoint depth and the inherited errors of the GFS some evidence of misrepresentation of wave spectra by the JONSWAP approach was also observed.

In order to improve the accuracy and predictability of extreme events, such as the one described here, it is imperative to increase the number of buoys and other platforms for in situ data collection along the Brazilian coast. We also recommend further investigations regarding the accuracy of the GFS along the Brazilian coast and the influence of heat fluxes in explosive cyclogenesis in Brazil. The Bergeron classification proved to be accurate in detecting Southern Brazilian explosive cyclones.

Data Availability Statement: Buoy data is available at <https://simcosta.furg.br/home>.

## Acknowledgments

This work was financially supported by OceanPact Serviços Marítimos S.A., Finep and the CRONOS Project. We would also like to gratefully thank the Brazilian Coastal Monitoring System (SiMCosta) for providing the buoy data applied in this work and for their technical support. This research was funded by Finep, grant number 0465/18. The APC was funded by OceanPact Serviços Marítimos S.A. MK, V.G.P. and R.B. acknowledge grants from FAPESP (2021/04128-8) and FUSP (2017/00686-0).

## References

- ALLEN, J.T.; PEZZA, A.B.; BLACK, M.T. Explosive cyclogenesis: a global climatology comparing multiple reanalyses. *Journal of Climate*, v. 23, n. 24, p. 6468-6484, 2010.
- ARAUJO, C.E.S.; FRANCO, D.; MELO, E.; PIMENTA, F. Wave regime characteristics of the southern Brazilian coast. In **Proceedings of the Sixth International Conference on Coastal and Port Engineering in Developing Countries**, Colombo, Sri Lanka, v. 4, p. 15-19, 2003.
- BITENCOURT, D.; FUENTES, M.; CARDOSO, C. Climatology of explosive cyclones over cyclogenetic area of South America. *Revista Brasileira de Meteorologia*, v. 28, n. 1, p. 43-56, 2013. doi
- BUI, H.; SPENGLER, T. On the influence of sea surface temperature distributions on the development of extratropical cyclones. *Journal of the Atmospheric Sciences*, v. 78, n. 4, p. 1173-1188, 2021. doi
- BURONE, L.; FRANCO-FRAGUAS, P.; CARRANZA, A.; CALLIARI, D.; MICHAELOVITCH DE MAHIQUES, M.; *et al.* Physical drivers and dominant oceanographic processes on the Uruguayan margin (southwestern Atlantic): a review and a conceptual model. *Journal of Marine Science and Engineering*, v. 9, n. 3, p. 304, 2021. doi
- CAMARGO, R.; TODESCO, E.; PEZZI, L.P.; DE SOUZA, R.B. Modulation mechanisms of marine atmospheric boundary layer at the Brazil-Malvinas confluence region. *Journal of Geophysical Research: Atmospheres*, v. 118, n. 12, p. 6266-6280, 2013. doi
- CASTRO, B.M.; MIRANDA, L.B. Physical oceanography of the western Atlantic continental shelf located between  $4^\circ\text{ N}$  and  $34^\circ\text{ S}$ -Coastal segment (4W). *Sea*, v. 11, p. 209-251, 1998.
- CUCHIARA, D.C.; FERNANDES, E.H.; STRAUCH, J.C.; WINTERWERP, J.C.; CALLIARI, L.J. Determination of the wave climate for the southern Brazilian shelf. *Continental Shelf Research*, v. 29, n. 3, p. 545-555, 2009.
- CAVALCANTI, F.A.; FERREIRA, N.J.; DIAS, M.A.F.; JUSTI, M.G.A. **Tempo e Clima no Brasil**. São Paulo: Oficina de Textos, 464 p., 2009.
- DE LIMA, A.D.S.; KHALID, A.; MIESSE, T.W.; CASSALHO, F.; FERREIRA, C.; SCHERER, M.E.G.; BONETTI, J. Hydrodynamic and waves response during storm surges on

- the southern Brazilian coast: a hindcast study. **Water**, v. 12, n. 12, p. 3538, 2020. [doi](#)
- GUACHAMIN-ACERO, W.; LI, L.; GAO, Z.; MOAN, T. Methodology for assessment of the operational limits and operability of marine operations. **Ocean Engineering**, v. 125, p. 308-327, 2016. [doi](#)
- GUACHAMIN-ACERO, W.; LI, L. Methodology for assessment of operational limits including uncertainties in wave spectral energy distribution for safe execution of marine operations. **Ocean Engineering**, v. 165, p. 184-193, 2018. [doi](#)
- GOKSU, S.; ARSLAN, O. Quantitative analysis of dynamic risk factors for shipping operations. **Journal of ETA Maritime Science**, v. 8, n. 2, p. 86-97, 2020. [doi](#)
- GYAKUM, J.R.; DANIELSON, R.E. Analysis of meteorological precursors to ordinary and explosive cyclogenesis in the western north pacific. **Monthly Weather Review**, v. 128, n. 3, p. 851-863, 2000. [doi](#)
- KHALID, A.; DE LIMA, A.D.S.; CASSALHO, F.; MIESSE, T.; FERREIRA, C. Hydrodynamic and wave responses during storm surges on the southern Brazilian coast: a real-time forecast system. **Water**, v. 12, n. 12, p. 3397, 2020. [doi](#)
- KOMEN, G.J.; CAVALERI, L.; DONELAN M.; HASSELMANN, K.; HASSELMANN, S.; JANSSEN, P.E.A.M. **Dynamics and Modelling of Ocean Waves**, 1st ed.; Cambridge: Cambridge University Press, 1994.
- KUO, Y.-H.; REED, R.J.; LOW-NAM, S. Effects of surface energy during the early development and rapid intensification stages of seven explosive cyclones in the Western Atlantic. **Monthly Weather Review**, v. 119, n. 2, p. 457-476, 1991.
- LIM, E.P.; SIMMONDS, I. Explosive cyclone development in the Southern Hemisphere and a comparison with Northern Hemisphere events. **Monthly Weather Review**, v. 130, n. 9, p. 2188-2209, 2002.
- HOSKINS, B.J.; HODGES, K.I.A. New perspective on Southern Hemisphere storm tracks. **Journal of Climate**, v. 18, n. 20, p. 4108-4129, 2005.
- MÖLLER, O.O., JR.; PIOLA, A.R.; FREITAS, A.C.; CAMPOS, E.J.D. The effects of river discharge and seasonal winds on the shelf off southeastern South America. **Continental Shelf Research**, v. 28, n. 13, p. 1607-1624, 2008.
- OHZ, A.; KLEIN, A.H.F.; FRANCO, D. A multiple linear regression-based approach for storm surge prediction along south Brazil. In: **Climate Change, Hazards and Adaptation Options**. Springer: Cham, pp. 27–50, 2020. [doi](#)
- PETERSON, R.G.; STRAMMA, L. Upper-level circulation in the South Atlantic Ocean. **Progress in Oceanography**, v. 26, p. 1-73, 1991.
- PEZZI, L.P.; SOUZA, R.B.; DOURADO, M.S.; GARCIA, C.A.E.; MATA, M.M.; SILVA-DIAS, M.A.F. Ocean-atmosphere in situ observations at the Brazil-Malvinas Confluence region. **Geophysical Research Letters**, v. 32, n. 22, p. 1-4, 2005. [doi](#)
- PEZZI, L.P.; DE SOUZA, R.B.; ACEVEDO, O.; WAINER, I.; MATA, M.M.; GARCIA, C.A.E.; DE CAMARGO, R. Multiyear measurements of the oceanic and atmospheric boundary layers at the Brazil-Malvinas confluence region. **Journal of Geophysical Research**, v. 114, n. D19, p. 1-19, 2009. [doi](#)
- PIOLA, A.R.; CAMPOS, E.J.D.; MÖLLER, O.O., JR.; CHARO, M.; MARTINEZ, C. Subtropical shelf front off eastern South America. **Journal of Geophysical Research**, v. 105, n. C3, p. 6565-6578, 2000.
- PIOLA, A.R.; PALMA, E.D.; BIANCHI, A.A.; CASTRO, B.M.; DOTTORI, M.; GUERRERO, R.A.; MARRARI, M.; MATANO, R.P.; MOLLER, O.O., JR.; SARACENO, M. Physical Oceanography of the SW Atlantic Shelf: A review. In: **Plankton Ecology of the Southwestern Atlantic**. Springer: Cham, p. 37-56, 2018.
- PIOLA, A.R.; MATANO, R.P. Ocean Currents: Atlantic Western Boundary-Brazil Current/Falkland (Malvinas) Current. In: **Encyclopedia of Ocean Sciences**, 3rd ed. Cambridge: Academic Press, pp. 414-420, 2019. [doi](#)
- REVELL, M.J.; RIDLEY, R.N. The origin and evolution of low-level potential vorticity anomalies during a case of Tasman Sea cyclogenesis. **Tellus A: Dynamic Meteorology and Oceanography**, v. 47, n. 5, p. 779-796, 1995. [doi](#)
- RODRÍGUEZ, M.G.; NICOLODI, J.L.; GUTIÉRREZ, O.Q.; LOSADA, V.C.; HERMOSA, A.E. Brazilian Coastal Processes: Wind, Wave Climate and Sea Level. In: **Brazilian Beach Systems**. Cham: Springer, v. 17, p. 36-46, 2016. [doi](#)
- SANDERS, F.; GYAKUM, J.R. Synoptic-dynamic climatology of the “Bomb”. **Monthly Weather Review**, v. 108, n. 10, p. 2725-2730, 1980.
- SELUCHI, M.; SAULO, A.C. Possible mechanisms yielding an explosive coastal cyclogenesis over South America: experiments using a limited area model. **Australian Meteorological Magazine**, v. 47, n. 4, p. 309-320, 1998.
- SHORT, A.D.; KLEIN, A.H.D.F. (Eds.) **Brazilian Beach Systems**. Cham: Springer International Publishing, pp. 37-66, 2016.
- STEVENSON, M.R.; DIAS-BRITO, D.; STECH, J.L. How do cold water biota arrive in a tropical bay near Rio de Janeiro, Brazil? **Continental Shelf Research**, v. 18, n. 13, p. 1595-1612, 1998.
- TOKINAGA, H.; TANIMOTO, Y.; XIE, S.-P.; TOKINAGA, H.; TANIMOTO, Y.; XIE, S. SST-induced surface wind variations over the Brazil-Malvinas Confluence: Satellite and in situ observations. **Journal of Climate**, v. 18, n. 17, p. 3470-3482, 2005. [doi](#)
- TOLMAN, H.L. **User Manual and System Documentation of WAVEWATCH-III Version 1.15**; NOAA/NWS/NCEP/OMB Technical Note; v. 151, 97 p, 1997.
- TOLMAN, H.L. **User Manual and System Documentation of WAVEWATCH-III Version 1.18**; NOAA/NWS/NCEP/OMB Technical Note; v. 166, 110 p, 1999.
- TOLMAN, H.L. **User Manual and System Documentation of WAVEWATCH III Version 3.14**; NOAA/NWS/NCEP/MMAB Technical Note; v. 276, 194 p, 2009.
- TSOPOURIDIS, L.; SPENSBERGER, C.; SPENGLER, T. Cyclone intensification in the Kuroshio region and its relation to the sea surface temperature front and upper-level forcing. **Quarterly Journal of the Royal Meteorological Society**, v. 147, n. 734, p. 485-500, 2020. [doi](#)
- WALLACE, J.M.; MITCHELL, T.P.; DESER, C.J. The influence of sea surface temperature on surface wind in the eastern equatorial Pacific: Weekly to monthly variability. **Journal of Climate**, v. 2, n. 12, p. 1500-1506, 1989. [doi](#)

- WAMDIG. The WAM model-A third generation ocean wave prediction model. **Journal of Physical Oceanography**, v. 18, n. 12, p. 1775-1810, 1988.
- WILCKEN, S. **Alpha Factors for the Calculation of Forecasted Operational Limits for Marine Operations in the Barents Sea**. Master Thesis, University of Stavanger, Stavanger, Norway, 2012.
- ZHANG, Z.; LI, X.-M. Global ship accidents and ocean swell-related sea states. **Natural Hazards and Earth System Sciences**, v. 17, n. 11, p. 2041-2051, 2017. [doi](#)

### Internet Resources

- ECMWF. [www.ecmwf.int/en/forecasts/datasets/archive-datasets/reanalysis-datasets/era5](http://www.ecmwf.int/en/forecasts/datasets/archive-datasets/reanalysis-datasets/era5), accessed in 2021, April, 09.

- NOAA. <https://www.ncdc.noaa.gov/data-access/model-data/model-datasets/global-forecast-system-gfs>.



License information: This is an open-access article distributed under the terms of the Creative Commons Attribution License (type CC-BY), which permits unrestricted use, distribution and reproduction in any medium, provided the original article is properly cited.